

Finite-Element Method Simulations of Guided Wave Phenomena at Terahertz Frequencies

Design of cylindrical-wire wave guides and other THz devices can be aided by finite element models that characterize propagation and interaction characteristics.

By JASON A. DEIBEL, *Member IEEE*, MATTHEW ESCARRA, *Student Member IEEE*,
NICHOLAS BERNDSEN, *Student Member IEEE*, KANGLIN WANG, AND
DANIEL M. MITTLEMAN, *Member IEEE*

ABSTRACT | As the science and engineering associated with terahertz time-domain spectroscopy and imaging evolves past the use of conventional free-space optics, the continued development of waveguides for terahertz pulses is increasingly relevant. The ability to model and simulate terahertz wave propagation aids in the development, visualization, and understanding of novel terahertz devices and phenomena. We discuss the use of the finite-element method, a powerful computational tool for the modeling of guided wave phenomena and devices at terahertz frequencies.

KEYWORDS | Finite-element method (FEM); photonic crystals; surface plasmon polaritons (SPPs); terahertz time-domain spectroscopy (THz-TDS); waveguides

I. INTRODUCTION

Terahertz time-domain spectroscopy and imaging are proven techniques for the characterization of semiconductors [1], [2], biomedical imaging [3], [4], and trace-gas detection [5]. There are potential applications for this broadband technology in fields such as security [6]–[9]

and quality-control in manufacturing [10], [11]. Terahertz time-domain spectroscopy (THz-TDS) systems use sub-picosecond pulses having a bandwidth that can span a large portion of the “terahertz gap” (100 GHz–30 THz). The generation of these broadband THz pulses is accomplished through the use of ultrafast lasers (pulses widths < 100 fs) in combination with either photoconductive antennas [12]–[14] or optical rectification in nonlinear optical crystals [15], [16]. Likewise, broadband detection is accomplished using ultrafast photoconductive antenna receivers [12], [14] or via electro-optic sampling [17].

A standard THz time-domain spectroscopy and imaging apparatus typically consists of an assembled system of free-space optical components that include lenses and mirrors for the guiding, focusing, and collimating of both the near-infrared laser radiation (NIR) and the terahertz radiation. The use of these bulky free-space optics hinders the development of THz technology due to the complexities associated with alignment of the optical components and the associated space requirements. As a consequence, the need for effective guided wave techniques has drawn considerable attention recently. The development of waveguides for use with terahertz pulses is complicated by the operational requirements of low attenuation loss and low dispersion, and by the lack of suitable materials with sufficient transparency at terahertz frequencies [18]. Several research groups have reported novel waveguiding structures including polymeric photonic crystal fibers [19]–[21], parallel-plate

Manuscript received March 16, 2007; revised April 17, 2007. This work was supported in part by the National Science Foundation, in part by the R. A. Welch Foundation, and in part by the Intelligence Community Postdoctoral Fellowship Program. The authors are with the Department of Electrical and Computer Engineering at Rice University, Houston, TX 77005 USA (e-mail: daniel@rice.edu).

Digital Object Identifier: 10.1109/JPROC.2007.898817

metal guides [22]–[24], low index discontinuity waveguides [25], and metallic slits [26]. We have recently described the use of bare metal wires, which can support a surface-guided wave with low attenuation and relatively little dispersion [18], [27]–[29]. This new class of terahertz waveguide is a promising step in the development of terahertz applications. In order for these waveguides to be implemented, it is vital that they be carefully characterized both theoretically and experimentally.

The finite-element method (FEM) is a useful and powerful computational technique for modeling how electromagnetic waves propagate and interact with their surroundings. With the FEM, one can determine propagation characteristics such as loss and dispersion and electromagnetic field distributions as a function of spatial location, frequency, or time. Advances in computer technology and the availability of commercial FEM software have lowered barriers to the use of the FEM for modeling of electromagnetic wave phenomena. As FEM modeling has been applied to study electromagnetic propagation in both the microwave and optical portions of the spectrum [30]–[32], it is a logical step to use this technique for the study of wave propagation at terahertz frequencies.

In this paper, we discuss the applicability of FEM simulations to the study of terahertz guided wave phenomena. We present a brief overview of the FEM technique and describe the critical aspects of modeling electromagnetic wave propagation and interaction at terahertz frequencies. Simulations of the excitation of terahertz surface waves on metal wire waveguides are presented. Next, we show how FEM modeling is used to develop and test a novel photoconductive antenna with radial symmetry that greatly enhances the coupling efficiency of THz radiation to wire waveguides. Finally we discuss the emission of THz radiation at the end of the wire waveguide.

II. FINITE-ELEMENT METHOD MODELING OF ELECTROMAGNETIC WAVE PROPAGATION

A. Basic Steps of Finite-Element Method Modeling

At its most basic level, the FEM provides an approximate solution to a system of linked partial differential equations. The FEM was first introduced by Courant in 1943 and its development has matched the pace of the growth of computer technology [33]. It was not until the 1960s that the FEM was applied to the problem of electromagnetic wave propagation when it was used to analyze waveguide modes [34]. As the focus of this paper is on the study of terahertz wave phenomena and devices using the FEM and not an explanation of the functionality of the FEM, it is recommended that the reader consult Jin's and Zimmerman's work for a more detailed explanation of the FEM [35], [36].

The completion of an FEM model of any type of electromagnetic phenomena generally involves several stages. The first is the definition of the model geometry. It can be as simple as defining the parallel plates of a capacitor or as complex as a coaxially fed patch antenna. An essential component of this stage is the definition of the simulation domain. This domain bounds the spatial extent of the simulation whether it is in one, two, or three dimensions. Within the simulation domain, it may be subdivided into smaller spatial extents known as subdomains.

Following the geometry definition, physical properties are assigned to the model. Material parameters such as the dielectric permittivity, the magnetic permeability, the refractive index, or the conductivity are defined for each subdomain. For each plane, edge, and point in the model domain, boundary conditions are assigned. These boundary conditions can include defining a boundary plane as a continuous boundary, a perfect electrical conductor, or a transition impedance boundary condition. Sources are defined at this point. For a dc electrostatics simulation, a boundary can be given a voltage potential whereas for a waveguide simulation, the boundary can be assigned an electric field source such as a port condition where a TE or TM mode is excited.

The next stage in the FEM modeling process is the discretization of the simulation domain. This spatial region is subdivided into numerous discrete elements that are much smaller than the subdomains that make up the simulation domain. The ensemble of all of these elements in the domain is often referred to as the mesh. The geometric nature of the mesh elements is a function of the dimension of the simulation i.e., triangular and rectangular mesh elements for 2-D simulations and tetrahedral and block elements in 3-D simulations. A system of nodes arises from the creation of the mesh. Interpolation functions are defined between the nodes that are chosen to approximate the solution. This node system, in conjunction with the previously defined physical parameters and boundary conditions, forms a system of partial differential equations (PDEs).

The system of PDEs must be solved in order to determine the electromagnetic fields within the simulation domain. Depending on the size and complexity of the simulation, the model solution can be arrived at using either direct solvers such as UMFPACK or SPOLES or iterative solvers such as GMRES [37]–[39]. While most FEM simulations are completed in the frequency-domain, time-domain modeling is also possible [40], [41]. The computational time required to solve the system of PDEs and arrive at a solution varies with the dimension of the simulation, the number of mesh elements, and the type of electromagnetic phenomena being modeled. Once a solution is found, parameters such as the electric field, magnetic field, capacitance, etc., can be plotted and analyzed.

B. Electromagnetic Wave Propagation Modeling Issues

The modeling of electromagnetic wave propagation can be quite challenging. To properly simulate wave propagation, the largest mesh element size must be no larger than one-third of the radiation's wavelength. Many models require an even higher mesh resolution constraining the largest mesh element to one-tenth of the radiation wavelength [36]. For the latter case, to model a wave propagating at a frequency of 100 GHz, the largest mesh element can be no larger than $300 \mu\text{m}$; for a wave at 1 THz, this critical element size shrinks to $30 \mu\text{m}$. However, a real-world model can involve feature sizes not only that small but also as large as centimeters. Thus a small critical mesh element size results in a model with a huge number of mesh elements. The number of mesh elements not only affects the computational requirements of the simulation, but can also determine whether or not a solution can be determined.

C. Computational Requirements

FEM simulations can be performed on any personal computer or workstation that is capable of running mathematical software packages such as Matlab. As with most computational techniques, the time required by an FEM solver to arrive at a solution ("the solution time") decreases with increasing processor speed. With some computational techniques such as the finite-difference time-domain method, the use of multiple processors in a parallel computing arrangement can greatly decrease the solution time. FEM solvers are difficult to implement across parallel computing geometries [42]. The primary computer component that governs FEM simulations is the RAM memory. As an FEM model's total number of mesh elements increases, the system of PDEs grows as well, thus increasing the RAM memory required for the computer to be able to solve the model. The advent of 64-bit computing technology and multiprocessor systems that allow the assignment of 8 GB of RAM per processor has significantly advanced the capabilities of FEM modeling as more complex models with larger mesh densities can be now be solved. In addition, new solvers such as the Pardiso [43], [44] solver are being developed that enable FEM simulations to be completed using parallel processing.

D. Commercial FEM Software

Commercial FEM software did not exist for the several decades following its first description in 1943 [33]. Even with the advent of the personal computer and the computer workstation, FEM simulations could only be accomplished by those who understood the mathematical intricacies of the method and could develop the necessary computer code to run the simulations. These limitations hindered the application of the FEM for electromagnetic device development and the understanding of novel phenomena. There is now a vast array of

commercially available FEM software packages to choose from (HFSS, ANSYS, ANSOFT, COMSOL Multiphysics). Several of these offer graphical user interfaces (GUIs) that allow the user to visually construct the simulation domain and to perform postprocessing of the solution. Commercial FEM software for electromagnetics simulations can vary from versions that only solve for one specific type of problem such as electrostatics or wave propagation to ones that can solve a wide variety of electromagnetics problems. Programs such as COMSOL Multiphysics allow the user to couple multiple application modes together [45]. In this paper, all of the simulations were performed using the COMSOL Multiphysics package.

III. MODELING THE EXCITATION OF THz SURFACE WAVES ON METAL WIRE WAVEGUIDES

A. Metal Wire Waveguide Experimental Configuration

In our early work with the metal wire waveguides, the radial mode of the waveguide was excited via a scattering mechanism [18], [27]. In this method, horizontally polarized terahertz pulses, generated using a GaAs photoconductive antenna, are focused onto the 0.9 mm diameter stainless steel wire waveguide (Fig. 1). An identical stainless steel wire is placed perpendicular to the waveguide near the focal spot of the beam. A small portion of the radiation scattered at this intersection point excites the radially polarized surface wave that propagates along the surface of the metal wire. The radial polarization of the surface wave is due to the circular cross section of the metal wire, which causes the electric field of the weakly guided mode to point away from the surface. This radially polarized guided wave is known as a Sommerfeld wave [46], [47] and is equivalent to an azimuthally polarized surface plasmon polariton (SPP). The SPP arises

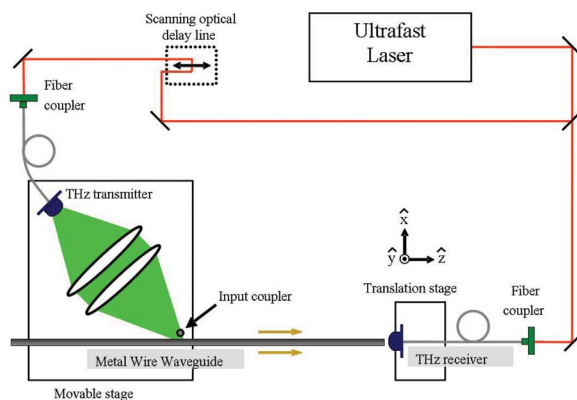


Fig. 1. Excitation of THz surface wave on a metal wire using a scattering configuration.

from the collective oscillations of the conduction electrons at the metal surface, in response to the driving electromagnetic surface wave [48]. The terahertz pulse is detected at the end of the wire with a fiber-coupled photoconductive receiver. The receiver used here was a conventional bow-tie antenna, sensitive only to the polarization component oriented parallel to the bow-tie axis [49]–[51]. As the THz radiation propagates along the surface of the wire waveguide, there is no terahertz field present at the central axis at the end of the wire. Detection measurements are consequently performed at lateral offsets from the central axis.

B. Finite-Element Method Model

Experimental results from the coupling configuration described in Fig. 1 indicate that less than 1% of the power of the incident terahertz beam is coupled to the wire waveguide by the scattering process described above. A more accurate estimate of the coupling efficiency is required. We have developed an FEM model of the dual-wire THz coupler that demonstrates the nature of the coupling and that also provides a method to more accurately quantify the coupling efficiency. The wire waveguide is modeled in three dimensions, with the outer surface of the metal wire defined as a perfect electrical conductor (PEC). To correctly model the ohmic loss of the waveguide, it would be necessary to consider the surface impedance of the wire's outer boundary and the Drude conductivity of the metal [18]. However, at this point our focus is on modeling the coupling efficiency of the experiment and not to consider the waveguide's inherent loss.

Fig. 1 shows the experimental configuration used to measure the waveguide properties. The coupler wire, having the same diameter and boundary conditions as the waveguide wire, is placed in the vicinity of the wire waveguide, but in a direction perpendicular to it. The distance between the closest outer surfaces of the two wires is $500\ \mu\text{m}$. The incident linearly polarized terahertz field is modeled as a plane wave whose \mathbf{k} -vector is incident at a 45° angle from the axis of the wire waveguide. This angle of incidence is chosen based on qualitative experimental results indicating that this geometry optimizes the input coupling. The propagation direction of the plane wave is chosen so that its center is incident at the center of the gap between the waveguide and coupler wires. The size of the plane wave (2 cm diameter) mirrors the size of the loosely focused terahertz beam used in the waveguide coupling experiment. The vector of the linear input polarization lies in the same plane (xz plane) occupied by the long axis of the wire waveguide, again mirroring the experiment. The simulation domain is bounded by a box of air confining the waveguide and coupler wires and the input plane wave. A low-reflecting boundary condition is selected for the outer walls of the domain so that any back reflections of

the EM waves in the simulation are minimized. An absorbing boundary condition or perfectly matched layer would be more physically accurate, but is not used for these simulations due to the modeling complexities and computational constraints introduced through their either implementation [36].

The 3-D simulation domain is discretized into approximately 1.8 million tetrahedral mesh elements yielding a computational model consisting of 2.1 million degrees of freedom. The large number of mesh elements is due to the mesh density constraints that are a function of the radiation wavelength, as noted above. The experiment is simulated using a time-harmonic solver, so that only one input frequency is considered at a time. The model problem is solved using an iterative generalized minimal residual (GMRES) iterative solver with symmetric successive overrelaxation (SSOR) matrix preconditioning [39], [45]. For a waveguide 15 cm long, a workstation with dual 64-bit processors and 14 GB of RAM arrives at a solution in less than 20 h. The solution time could be lessened with the use of a geometric multigrid preconditioner, which was unavailable at the time when these simulations were performed. The multigrid technique employs a hierarchy of meshes each with different mesh densities [52]. Solution time is decreased as the software algorithms only employ the fine mesh when necessary and otherwise use coarser meshes when appropriate.

C. FEM Simulation Results

Simulation results completed for a frequency of 0.1 THz are presented in Fig. 2 [53]. The incident plane wave is scattered at the gap between the wire coupler and waveguide. It is evident that the majority of the plane wave propagates unimpeded and only a small amount of the incident radiation is coupled to the radial mode of the waveguide. Fig. 3 is a plot of the x -component of the electric field at a point $300\ \mu\text{m}$ above the wire and along its z -axis. The large peak located at $z = 0$ is part of the incident excitation wave. A sine wave with a frequency of 0.1 THz is fit to the oscillating electric field along the waveguide, demonstrating that the model is successfully simulating wave propagation. Both forward and backward propagating modes are excited. Since the wires are modeled as PECs, we expect little attenuation once the mode is excited, which is consistent with the results of the calculation. Any noise or amplitude fluctuation present in the plot in Fig. 3 is due to an insufficient mesh density which is limited by the computational capabilities of the simulation computer. A plot of the x -component of the guided wave's electric field at the end of the wire (xy plane) is shown in Fig. 4(a). It is compared to experimental data in Fig. 4(b). The spatial profile of the electric field at the end of the waveguide is measured by translating the THz receiver antenna in the plane normal to the waveguide axis [27]. The two-lobed structure is what one would expect in observing a radially symmetric

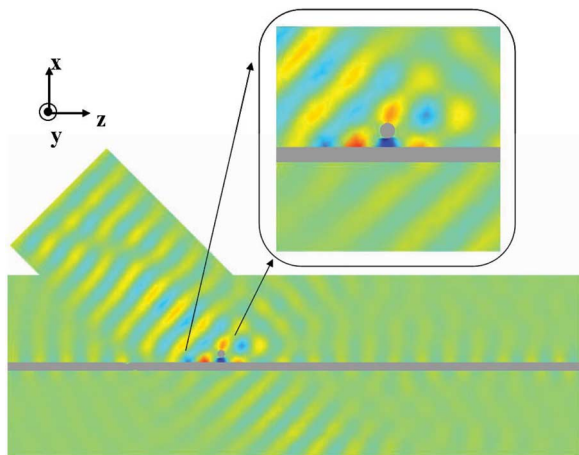


Fig. 2. FEM simulation result of a 0.1 THz wave coupling to a wire waveguide using a dual-wire coupling configuration (E_x shown here). The inset shows a zoomed-in view of the electric field (xz plane) in the coupling region between the two wires.

polarization pattern with a polarization-sensitive detector. Thus, this result demonstrates the radial nature of the waveguide mode.

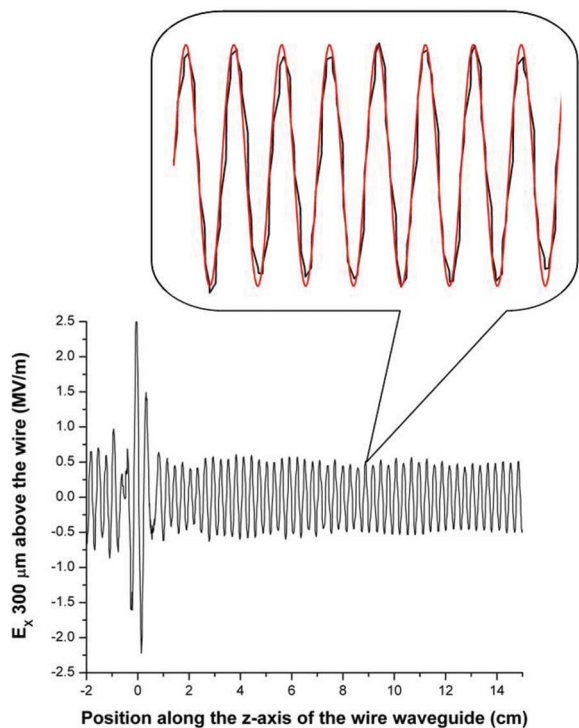


Fig. 3. A plot of the x -component of the electric field along a line 300 μm above the wire and parallel to the axis. The inset shows a 0.1 THz sine wave fit to the extracted simulation data.

The simulation results demonstrate the propagation of a surface wave, or SPP, supported by the wire waveguide. The boundary condition chosen for the surface of the wires is a perfect electrical conducting (PEC) condition, meaning that the model treats the volume bounded by the surface of the wire as if its conductivity were infinite. However, the Sommerfeld model predicts that a PEC wire cannot support a stable radial mode [46], [54]. Due to limits on the size of the simulation domain imposed by computational capabilities, we can only model propagation along less than 15 cm of wire. This distance may not be long enough to adequately determine whether or not the propagating mode is stable and is supported by the waveguide. While the length of the wire (z) in our simulation is limited, a more important condition is imposed by the finite lateral (x and y) extent of the simulation domain which is also limited by computational capabilities. It is possible that the low-reflecting boundary conditions chosen for the outer walls of the simulation domain may perturb the simulation results. Future simulations replacing the low-reflecting boundary condition with a perfectly matched layer or absorbing boundary condition would potentially yield insight into this aspect of our simulation results. Furthermore, it is not possible from these simulation results to determine if single-mode excitation is taking place. The surface waves seen in the simulation can be described as a superposition of many modes, all but one of which exhibit extremely high radiation losses [46]. While these FEM simulations do not demonstrate the excitation of stable single-mode propagation along the waveguide, they do effectively demonstrate the coupling of terahertz radiation to the waveguide.

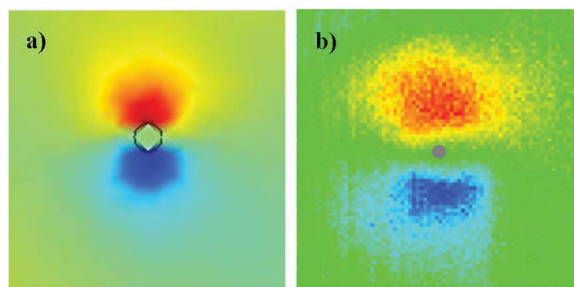


Fig. 4. (a) FEM simulation results a 0.1 THz continuous wave showing the x -component of the electric field at the end of the metal wire waveguide (0.45 mm radius) (xy plane shown). (b) Experimental measurements showing the spatial profile of the electric field at the end of metal wire waveguide (0.45 mm radius). This image is obtained by translating the THz receiver antenna in the plane normal to the waveguide axis. This data represents a spectrum-weighted average as all of experimental data was obtained at the same time-delay. Red indicates positive values and blue indicates negative values of the electric field. The polarity reversal shown in both figures is evidence of the radial nature of the waveguide mode.

It is now quite simple to quantify the coupling efficiency at 0.1 THz. In our model geometry, the incident excitation wave is defined at the base of a cylinder that can be seen in Fig. 2. The input power is determined by integrating the time-averaged power over the area defined by the circular base of the cylinder, where the input wave is excited. Likewise, the power coupled to the waveguide mode is calculated by integrating the time-averaged power over a circular area normal to the z-axis at the end of the waveguide (15 cm from the point of excitation). These calculations produce a simulated power coupling efficiency for the dual wire coupling configuration of 0.42%, comparable to the estimate generated from experimental data [18]. It should be noted that this number is probably the upper limit on any expected coupling efficiency. The wires in this simulation were modeled as PECs, so no loss due to finite conductivity was considered. Also, while the efficiency is expected to vary with wavelength, wire separation, etc., there is no reason to expect it to increase greatly, since the polarization of the waveguide mode and the incident wave are so poorly mismatched. It is important to note that it is virtually impossible to develop a closed-form analytical approach that would produce the coupling efficiency. The versatility and utility of the FEM approach provides a convenient method of modeling laboratory results of this sort.

IV. ENHANCED COUPLING OF THz RADIATION TO METAL WIRE WAVEGUIDES

A. A Photoconductive THz Antenna With Radial Symmetry

In order to address the low coupling efficiency associated with the early terahertz metal wire waveguide experiments, the poor spatial overlap between a linearly polarized THz source and the radial mode of the waveguide must be addressed. Prior to 2004, standard methods of THz pulse generation, such as photoconductive antennas or optical rectification, produce linearly polarized light [55]. Nahata *et al.* addressed the coupling problem via modification of the waveguide itself [56]. We have focused our efforts on developing a novel photoconductive terahertz antenna with radial symmetry that can adequately address the coupling issue [47], [53], [57].

Traditional photoconductive antenna design employs a linear dipole configuration or similar, resulting in linearly polarized pulses. We instead have proposed an antenna with a cylindrical symmetry to produce a “radial array” of Hertzian dipoles (Fig. 5). A short optical pulse excites the region between the two dc-biased electrodes creating an annular current surge induced by the acceleration of the photogenerated carriers in the illuminated region. As the electrode patterns on photoconductive antennas are typically photolithographically defined on the semicon-

ductor substrates in a cleanroom environment, terahertz antenna fabrication can be time consuming and financially costly. Trial-and-error development and testing of novel antenna designs is not cost-effective. In a situation such as this one, where novel antenna designs are being developed to function with novel waveguide designs, it is extremely beneficial to model the new antenna designs and waveguide configuration prior to device fabrication and testing. We show that the FEM is an important design tool in the development of novel terahertz antenna and waveguides.

B. Analytical Model

Both analytical methods and FEM simulations show that an idealized radial antenna can produce a radially polarized terahertz beam [57]. The idealized radial antenna ignores the effects of the feed electrode and the break in the outer electrode present in the actual design (Fig. 5). A simple calculation illustrates the principle of a “radial array” of Hertzian dipoles. Neglecting the influence of the dielectric substrate, the radiated field can be thought of as a superposition of a large number of dipole fields, emitted by a series of point dipoles distributed on a circle, each pointing radially away from the origin. The field from each one of these point dipoles can be found by simply shifting and rotating a classical far-field dipole pattern [58]. The radiated power is computed using superposition, as

$$P \approx \frac{1}{2} \text{Re}[\vec{n} \cdot (\vec{E} \times \vec{H}^*)] \\ = \frac{1}{2} \text{Re} \left[\vec{n} \cdot \left(\sum_i^N \vec{E}_i \times \sum_i^N \vec{H}_i^* \right) \right] \quad (1)$$

where \vec{E}_i and \vec{H}_i are the electric and magnetic fields for each dipole element. Fig. 6 shows the results of this computation (solid curve) completed at the single frequency

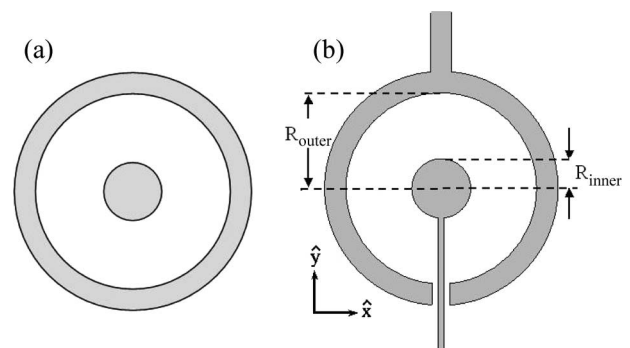


Fig. 5. (a) A schematic of the ideal radially symmetric antenna pattern. (b) A schematic of the actual radially symmetric antenna design.

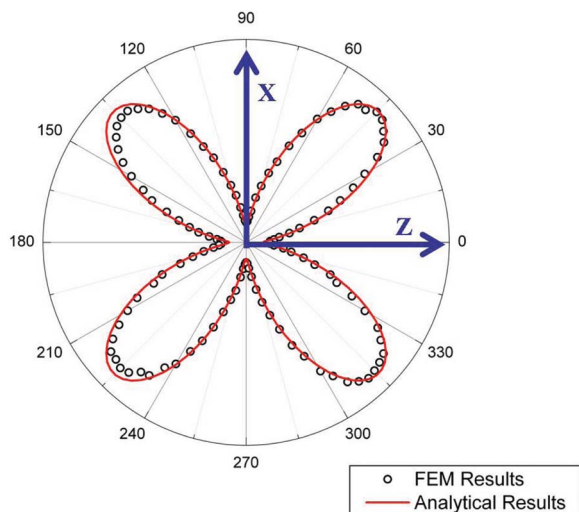


Fig. 6. The calculated far-field radiation pattern in the xz plane, neglecting substrate effects. The solid horizontal line indicates the z axis, which is the rotational symmetry axis of the antenna. The open circles show the results of the FEM simulations.

of 1 THz. It is evident that no radiation is emitted in the plane of the antenna or along the axis of cylindrical symmetry perpendicular to the plane of the antenna. By rotating this result around this symmetry axis, one obtains the full three-dimensional far-field radiation pattern, clearly a “donut” mode, as expected for radially polarized emission.

C. FEM Simulation of an Idealized Radial Antenna

The analytical model described above is adequate for describing the emission from an idealized radial antenna in free-space. However, it can not easily be modified to account for the effect of a dielectric substrate. To verify the analytical model and account for the effects of a high dielectric substrate, we model the ideal antenna design and its generated electric field pattern using the FEM. A current distribution is defined in the yz plane (the plane of the antenna) in a disc-shaped domain centered at the origin and bounded by an inner (R_{inner}) and outer radius (R_{outer}). The annular current pattern of the antenna is modeled by assigning a time-varying current to this disc

$$\vec{J} = \left[\left(\frac{x}{r} \alpha e^{-\beta r} \right) \hat{x} + \left(\frac{y}{r} \alpha e^{-\beta r} \right) \hat{y} \right] \epsilon_0 j \omega e^{j\omega t} \quad (2)$$

where α and β are constants chosen such that the magnitude of \vec{J} decays to zero at the outer edge of the disc. This current distribution is surrounded by a spherical surface in the far field of the antenna, on which the emitted field is computed [Fig. 7(a)]. Low reflecting boundary conditions are selected for the model domain boundaries in order to minimize reflections of the fields generated by the antenna. As with prior models, an absorbing boundary condition or perfectly matched layer is more physically appropriate, but is not chosen in order to minimize the computational load associated with the model. A mesh of approximately 60 000 elements is used

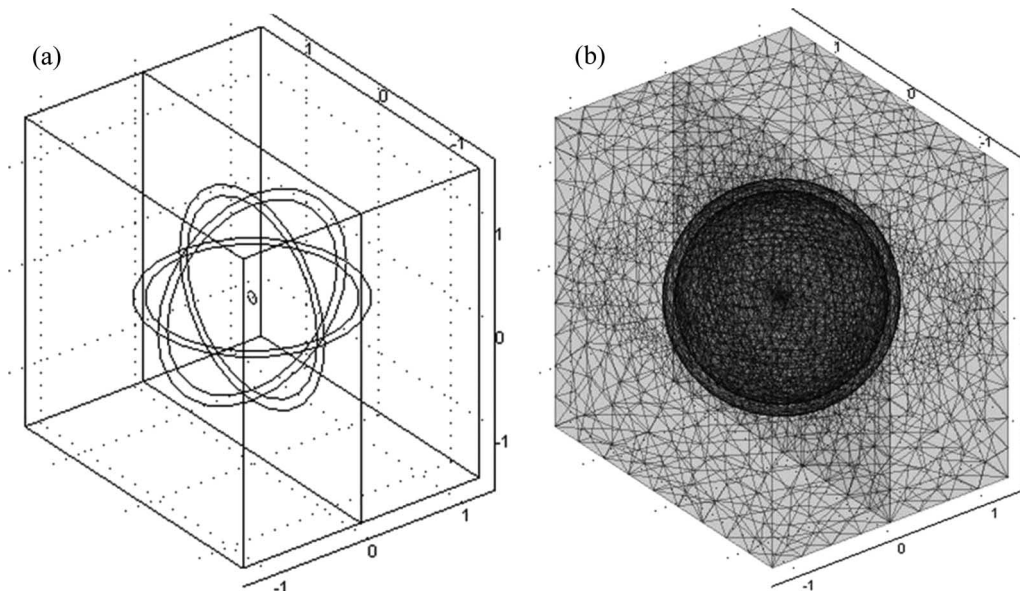


Fig. 7. (a) The model geometry of the FEM simulation of the idealized radial antenna. (b) The generated mesh from the same FEM simulation.

[Fig. 7(b)]. We first model the idealized radial antenna in free space, and then model the antenna situated on a dielectric half space. We have chosen a dielectric of $\epsilon = 12.25$, the approximate value for GaAs in the THz range. Due to the low absorption in GaAs at terahertz frequencies, the loss in the dielectric substrate is ignored [2]. A stationary linear direct solver (UMFPACK) was employed to solve the model and analyze the electromagnetic fields emitted by the antenna at a variety of frequencies for both the free-space and dielectric half-space models.

The results from the FEM simulations of the idealized radial antenna in free-space agree well with those from the analytical model previously described (see open circles in Fig. 6). Good agreement is observed in both the angle and width of the emitted lobe. Fig. 8(a) is a three-dimensional plot of the FEM simulation further demonstrating the radial polarization of the beam emitted by the simulated ideal antenna in free-space. In the case of an

antenna on a dielectric half-space, the lobed pattern is largely preserved, except that most of the energy is radiated into the substrate (greater than 98%) [Fig. 8(b)], similar to the effect observed for conventional dipole substrate antennas [59].

D. FEM Simulation of the Actual Radial Antenna

A Multiphysics approach is used for the FEM simulations of the radially symmetric terahertz antenna [Fig. 5(b)] [45]. With this approach, two linked simulations are performed one after another. The first simulation is a dc electrostatics model in which the dc electric fields present in the radial antenna gap are determined. The second simulation is an electromagnetic wave propagation model. The solution from the first simulation, which contains the static electric field in the gap area, is used as the amplitude in the time-varying excitation field for the wave propagation simulation. Both simulations rely on the same model geometry and mesh, but the physical parameters, boundary conditions, and master equations are different for each.

The paired simulations are run in 3-D. The radial antenna geometry is defined in a 2-D plane where the center of the antenna consists of a circular electrode $5 \mu\text{m}$ in diameter, fed by an electrode $1 \mu\text{m}$ wide that approaches the center from the negative y -axis direction. The separation between the center electrode and the $10 \mu\text{m}$ wide outer electrode is $100 \mu\text{m}$. There is a $7.5 \mu\text{m}$ gap on each side of the feed electrode at the bottom of the antenna where the outer ring electrode approaches the feed electrode. The boundaries of the electrodes are defined as PECs. The 2-D geometry containing the radial antenna structure is placed at the interface between a section of air and a 0.5 mm thick dielectric substrate, with a dielectric constant of 12.25 , approximately equal to that of GaAs. A substrate-matched hyperhemispherical silicon dome (2 mm radius) is placed on the other side of the GaAs substrate in order to couple the beam into free space and collimate it. This model configuration is chosen such that it closely mirrors a photoconductive antenna transmitter assembly commonly used in terahertz time-domain spectroscopy [60]. In order to adequately characterize the influence of the feed electrode on the radial antenna design, we also model an idealized radial antenna (with no feed electrode and no gap in the outer circular electrode) with a $100 \mu\text{m}$ radius on the same GaAs substrate with the same silicon dome configuration.

In the first dc electrostatics simulation, the outer electrode is grounded and a potential is assigned to the center electrode. A charge density with a Gaussian distribution and a $1/e$ width of $40 \mu\text{m}$ is defined at the center of the antenna. This is done to mimic the charge carriers generated in the GaAs by the optical pump pulse in a typical photoconductive generation scheme. The electrostatic fields are computed using the FEM solvers

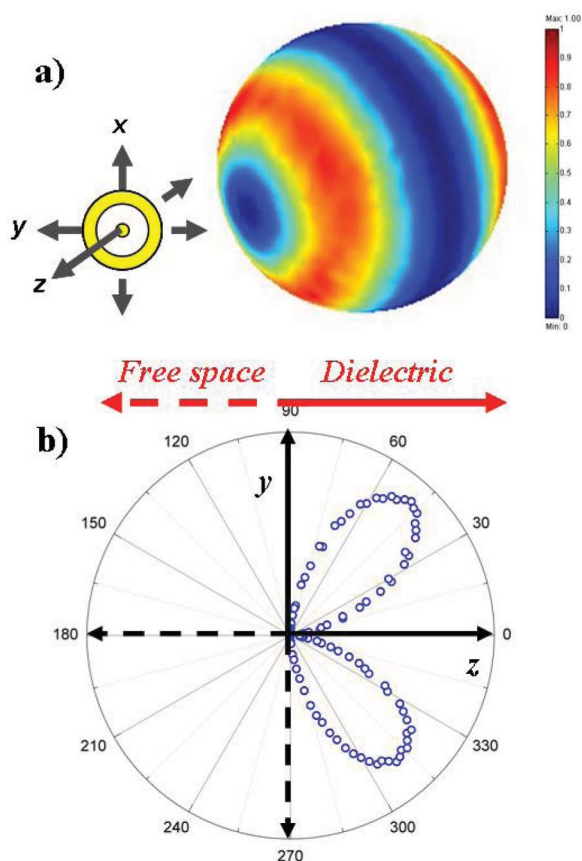


Fig. 8. (a) FEM simulation of the power emitted by an “ideal” radial antenna in free space at 0.5 THz. The antenna is located at the center of the sphere within the xy plane. (b) A polar plot of the radiation pattern for the radial antenna on a dielectric half-space, extracted from FEM simulation results. The vast majority of the power is radiated into the high dielectric substrate.

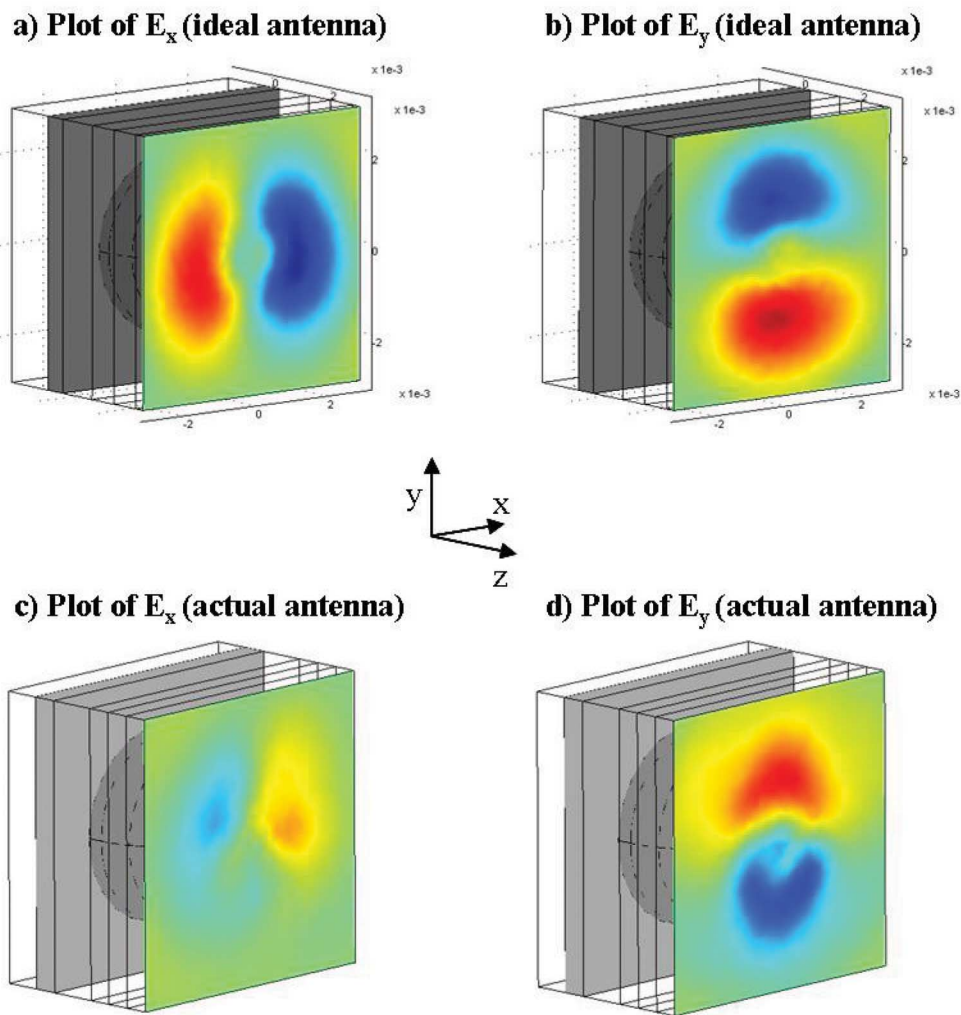


Fig. 9. FEM simulation results of the radial antenna in a typical THz configuration. (a), (b) Plots of the x and y component of the electric field for the idealized radial antenna. (c), (d) Plots of the x and y component of the electric field for the actual radial antenna.

and then those fields are used as the time-varying input fields for the electromagnetic wave propagation model. These models, both the ideal and the actual radial antenna devices, typically consisted of approximately 90 000 mesh elements and were run in less than 4 h on Pentium PC with 2 GB of RAM.

Fig. 9 shows the simulated radiation fields at 0.1 THz in the xy plane immediately after the silicon dome, which is visible in addition to the GaAs substrate. The FEM results show that the field from the idealized antenna is perfectly radial. The generated field from the actual radial antenna structure [Fig. 9(c) and (d)] is not perfectly radially polarized. This is due to the lack of symmetry in the actual antenna design. The break in the outer electrode and the presence of the feed electrode create asymmetry in the lower half of the antenna structure. This results in the y -component of the electric

field being stronger in amplitude than the x -component and the strongest parts of the x -component of the generated field not being centered on the antenna. The spatial overlap of the fields between these two sets of simulations (idealized antenna versus actual antenna) can be calculated. Approximately 60% of the power generated by the actual antenna emerges in the form of a radial mode.

E. Enhanced Coupling Capability

In order to fully evaluate the effectiveness of the radial antenna design prior to actual device fabrication, it is helpful to perform additional FEM simulations of the coupling capability of the radial antenna's output to a metal wire waveguide. The geometric models used in the previous simulations are modified to include the addition of a wire waveguide directly end-coupled to the center and

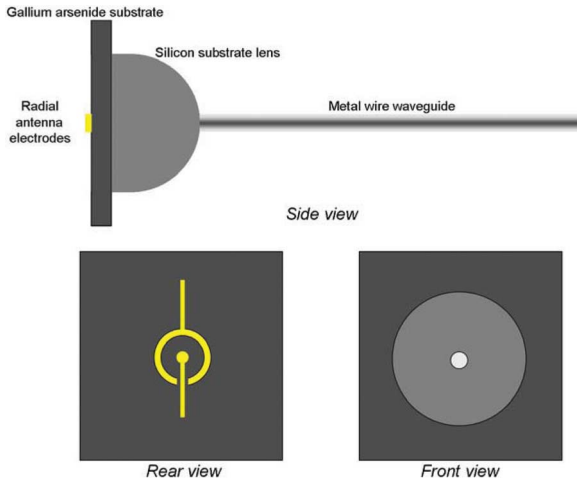


Fig. 10. Geometry of the FEM simulation model of radial antenna coupling to a wire waveguide.

exterior of the silicon domes (Fig. 10). The wire waveguide's dimensions, 0.9 mm diameter, are identical to the waveguides used in our previously published results [18], [27]. The wire waveguide is modeled as a PEC. For simulations involving the idealized antenna, the wire waveguide is 2.75 cm long; whereas those with the actual radial antenna design the waveguide is 1.75 cm long. This difference is a result of computer capability constraints, which limit the maximum number of mesh elements in any given model. Due to its more complex electrode structure, the radial antenna requires more mesh elements than the idealized antenna. Consequently, the wire waveguide is shortened in order for the simulation to be capable of realizing a successful solution.

Fig. 11 presents the results of FEM simulations performed at 0.1 THz of the idealized and actual radial antennas coupled to wire waveguides. The idealized antenna is clearly capable of exciting the low-order radial mode of the wire waveguide. Likewise, the actual antenna design is also shown to be capable of exciting the radial mode, although with somewhat lower efficiency. A more quantitative observation can be obtained by performing a coupling efficiency calculation similar to the one performed in Section III. The power available to be coupled into the waveguide is calculated by integrating the time-averaged power over a boundary in the xy plane immediately after the silicon dome. This is the same plane where the electric field is plotted in Fig. 9(c) and (d). The power coupled into the waveguide is determined in a similar manner. The time-averaged power is integrated over a boundary at the end of the waveguide and normal to it. The areas integrated over in both cases are identical. For the actual radial antenna design, this calculation yields a coupling efficiency of approximately

56%, an improvement of more than 2 orders of magnitude over the 0.42% coupling efficiency obtained via the scattering mechanism discussed earlier. Additional simulations with the waveguide removed were also performed and showed that, for both the case of the idealized and actual antenna structures, only a very tiny amount of power propagated to the end of the simulation domain.

Following this simulation work, radially symmetric photoconductive antennas were fabricated and tested [53]. A radially polarized mode was excited and guided over the length of a 27 cm wire waveguide. The magnitude of the peak terahertz electric field detected at the end of the waveguide was twenty times larger than the radiation detected at the same position with the waveguide removed. A quantitative comparison of the two coupling schemes presented here is difficult. In order to determine the coupling efficiency with either the scattering configuration or the radial antenna one, a single time-domain measurement at a single spatial location before and after

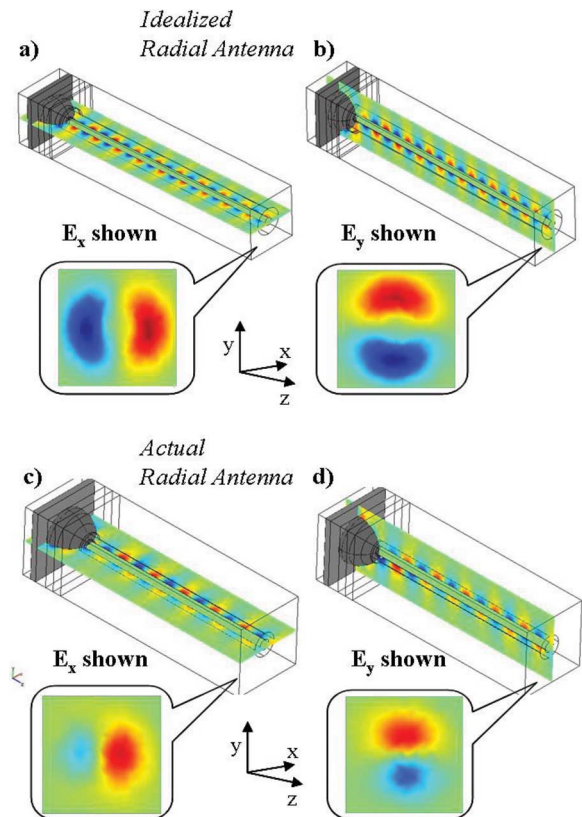


Fig. 11. FEM simulation model of radial antenna coupling to a wire waveguide. (a) Plot of E_x at the end of a waveguide coupled to an ideal radial antenna. (b) Plot of E_y at the end of a waveguide coupled to an ideal radial antenna. (c) Plot of E_x at the end of a waveguide coupled to an actual radial antenna. (d) Plot of E_y at the end of a waveguide coupled to an actual radial antenna.

the waveguide is not sufficient. To determine the experimental coupling efficiency, measurements of the total electric field over a large spatial region must be performed and are difficult and time-consuming. A more qualitative comparison of measurements from both coupling configurations shows that the signal-noise-ratio of the THz field measured at the end of the waveguide excited using the radial antenna is significantly higher than that of the field measured at the end of wire excited using the scattering configuration [18], [53].

It is noteworthy to stress again the importance of conducting the FEM simulations prior to antenna device fabrication and characterization. Our simulations of a radial antenna at an air-dielectric interface show that over 98% of the generated power is radiated into the dielectric [57]. The conventional substrate + matched silicon dome configuration that is modeled in our simulation geometry permits most of the power available to be coupled to the waveguide. Others have reported experimental results using a radial antenna similar in design to ours, but in a configuration involving optically pumping the antenna through the dielectric substrate [28], [47]. This significantly limits the amount of power available to be coupled to the waveguide because most of the emitted THz power is lost into the high dielectric substrate. While other methods of generating radially polarized THz radiation [61] and exciting the primary mode of metal wire waveguides [56] have been reported, the FEM simulations in conjunction with experimental characterization show that a properly designed photoconductive terahertz antenna can produce a radially polarized beam that couples very efficiently to the primary mode of a metal wire waveguide.

F. Second-Generation Radial Antenna

The knowledge and insight gained from the FEM simulations of the terahertz radial antenna suggests design enhancements that could be made to the antenna that would improve its ability to generate radially polarized light. From Fig. 9(c) and (d), it can be inferred that the presence of the feed electrode in the antenna structure can be blamed for the asymmetry in the generated terahertz electric field. We propose a design for a second-generation radial antenna that addresses this issue. The proposed design [Fig. 12(a)] relies on the addition of a 2nd feed electrode, placed directly opposite to the original feed electrode. The new design then possesses two breaks in the outer electrode structure, but now has symmetry about both x - and y -axes. This design also provides the ability to adjust the curvature of the outer ring electrodes in order to tune the emitted polarization.

The second-generation design is simulated in a manner very similar to the original design using the same 2 stage Multiphysics FEM approach. The simulated antenna structure consisted of a 10 μm diameter circular central

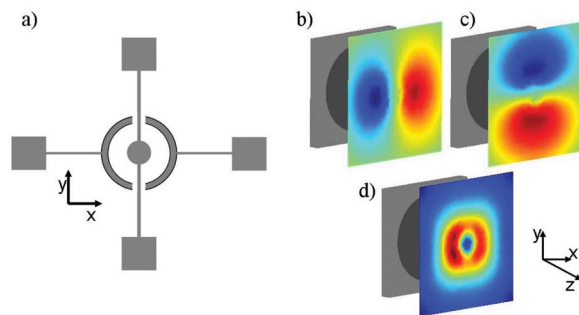


Fig. 12 (a) Electrode design of the second-generation photoconductive THz antenna with radial symmetry. (b) FEM simulation plot of the x -component of the electric field generated by the radial antenna. (c) FEM simulation plot of the y -component of the electric field generated by the radial antenna. (d) FEM simulation plot of the power generated by the radial antenna.

electrode fed above and below by 2 μm wide lines. The distance between the center electrode and the ring electrodes (10 μm wide) is 75 μm . As with the earlier simulations, the second-generation radial antenna is placed on a 0.5 mm thick GaAs substrate with a silicon substrate dome lens on the opposite side. Simulation results are plotted in Fig. 12(b) and (c). When examining both the generated x -component and y -component of the electric field, the polarity reversal and symmetry associated with radial polarization are evident. The improvement in the quality of the radial polarization emitted by the second-generation antenna is further established upon examination of a plot of its power emission [Fig. 12(d)]. Fabrication of these second-generation devices is currently under way.

V. THz EMISSION FROM METAL WIRE WAVEGUIDES

A. Motivation

In addition to the study of the excitation of terahertz surface plasmon polaritons on metal wire waveguides, it is also important to understand what happens when the THz radiation propagates to the end of the wire. In most of the reported experiments involving terahertz metal wire waveguides, the THz pulses are detected by allowing them to propagate to the end of the wire and emit into free-space [18], [27], [28], [47], [53], [56], [62], [63]. In order for experiments involving THz metal wire waveguides to be properly interpreted, it is necessary to characterize the spatial properties of this emitted THz radiation as it transitions from the near-field at the end of the cylindrical wire to the far-field. While experimental measurements are necessary to accomplish this, it is also essential that a theoretical model

of this near-field to far-field transition be developed. To our knowledge, closed-form analytical expressions that describe this near-field to far-field transition do not exist. As a result, numerical modeling can again play an important role.

Experimental characterization of the SPP emission at the ends of metal wire waveguides has found that the measured spectra of these terahertz pulses are spatially dependent [64]. Fig. 13 is a schematic of one type of such characterization experiment. Measurements are performed by varying the distance d between the detector and the end of the wire at a fixed transverse distance w . As the distance d is increased, the spectral maximum of the measured THz pulse shifts to higher frequencies. In addition, the peak amplitude of the spectrum decreases.

B. Frequency Dependent Diffraction

To better understand such experimental results, we again employ the FEM to simulate the propagation of a Sommerfeld wave [46] at THz frequencies along a metal wire waveguide and the subsequent emission of THz radiation into the far-field [64]. The model geometry consists of a 0.9 mm diameter waveguide, 2.5 cm

long placed inside of a cylindrical subdomain (3.75 cm in length, 6.5 mm in diameter) which bounds the volume of the simulation. The large simulation domain is necessary because a long extent of waveguide is required for the excited THz surface wave to exhibit stable propagation. Electric field excitation of the Sommerfeld wave is accomplished by assigning a time-varying electric field to one of the circular bases of the bounding cylinder. This excitation is based on an analytical solution describing the propagation of a Sommerfeld wave [46]. The external boundaries, with the exception of where the Sommerfeld wave is excited, are defined as “matched” boundaries which minimize the possibility of back reflections of any propagating electromagnetic waves. The metal surface of the wire waveguide is assigned a transition boundary condition that is dependent on the metal’s surface impedance and finite conductivity. The simulation mesh consists of over 1.5 million mesh elements. The solution is obtained using a time-harmonic iterative solver that employs a GMRES method with SSOR matrix preconditioning that solves for only one radiation frequency at a time [39]. A workstation with dual 64-bit processors and 16 GB of RAM typically arrives at a solution after 3 h of computational time. Computer limitations do limit the frequencies that can be simulated due to the increasing number of mesh elements required for simulations at higher frequencies. This issue is further complicated by the nearly 4 cm long simulation domain which also results in a large number of mesh elements.

The FEM simulation results provide an explanation of the aforementioned experimental measurements. Fig. 14 shows 2-D images of the calculated spatial distribution of the THz intensity at and around a 0.9 mm stainless steel wire, for a set of frequencies from 50 to 150 GHz. As expected, the images show that no radiation is present beyond the end of the wire along its axis. This is due to the fact that the waveguide mode is radially polarized, and therefore must vanish on the axis of symmetry. More importantly, the simulation results show that at the end of the wire, the spatial shape of the emitted field is a conical emission pattern propagating into free space. Inspection of this conical pattern reveals the presence of frequency-dependent diffraction at the end of the metal wire. The opening angle becomes smaller and the width of the conical pattern narrows with increasing frequency. Thus, the spatial size of the emitted beam at the end of the wire is broader at lower frequencies. This effect is a result of the terahertz surface waves scattering into propagating waves, which diffract off the edges of the cylinder surface. The diffraction is stronger for the low frequencies than for the high frequencies. Additional time-domain simulations are being conducted to determine if there is an end-face reflection of the THz surface wave at the end of the wire due to an impedance mismatch with free space. In this case, FEM simulations

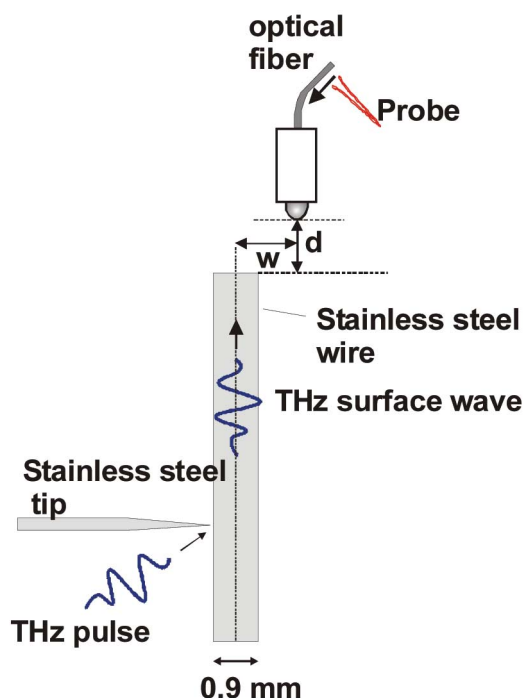


Fig. 13. Schematic diagram used to measure the THz electric field present near the end of a metal wire waveguide using fiber-coupled THz emitters and detectors. In these measurements, w is the transverse separation between the center of the waveguide and the position where the field is measured; d is the longitudinal distance.

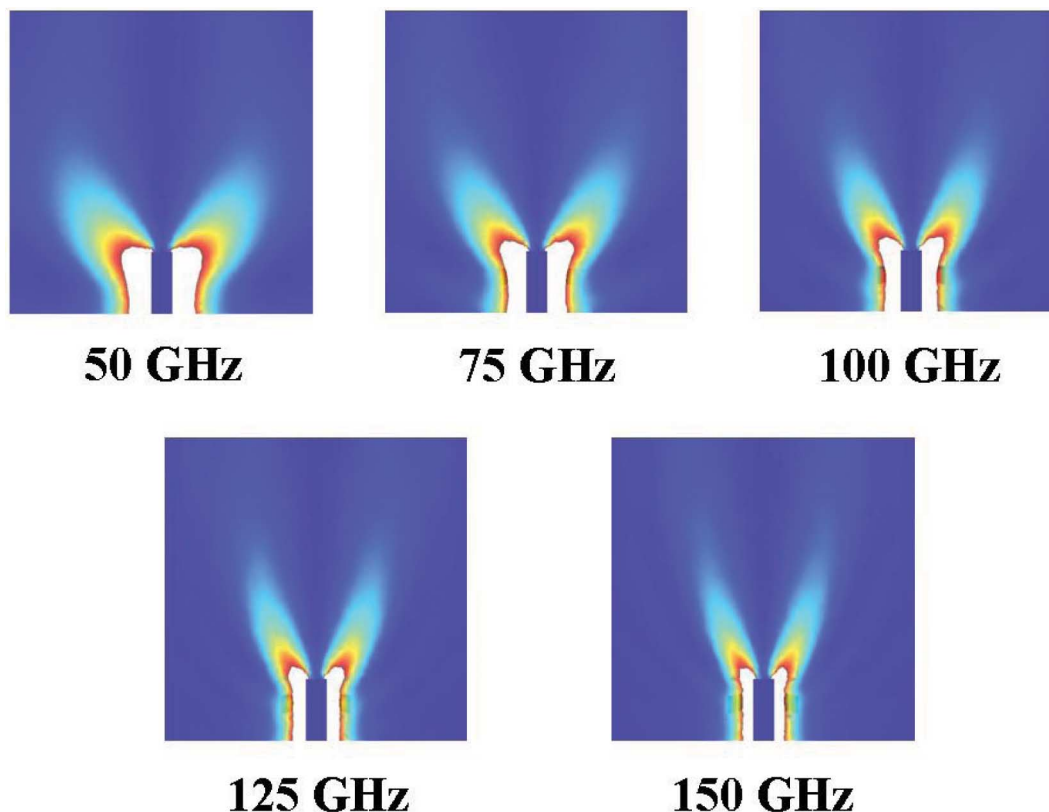


Fig. 14. Simulated THz intensity distribution in a plane containing the axis of a 0.9 mm thick wire, for five different frequencies. Red indicates a high intensity, blue indicates a low intensity. The color scale in these images has been saturated to enhance the visibility of the fields propagating away from the end of the wire. The higher intensities near the wire are therefore beyond the limits of this saturated color scale, and are depicted in white.

provided a visualization of the frequency-dependent diffraction at the end of a metal wire waveguide that aids in the interpretation of experimental results.

C. THz Emission From Tapered Wire Waveguides

A logical extension of this work is to modify the end geometry of the wire waveguide. Using an FEM model, we investigate the effect of tapering a metal wire waveguide to a tip size smaller than original diameter of the wire. The models consist of THz surface plasmon polaritons being excited at the beginning of a 1.5 cm long section of parallel wire with a 0.9 mm diameter that slowly tapers down to much smaller tip diameters. Fig. 15 shows FEM simulation results of various tip diameters at differing frequencies. Diffraction of the emitted terahertz wave still occurs at the end of the tapered wire waveguide. It is further evident that the spatial extent of the field at the end of the wire can be manipulated by varying the diameter of a tapered wire waveguide. The spatial extent of the field narrows with decreasing tip diameters, as the propagating mode is adiabatically compressed. The ability to manipulate the spatial extent of the field

emanating from a wire waveguide provides a promising direction for the future use of wire waveguides in terahertz microscopy. In fact, recent simulations discussed by Maier *et al.* have shown that periodic corrugations on tapered metal wire waveguides can further confine the terahertz field [65].

Tapered waveguide geometries have been utilized for various applications and radiation frequencies for many years [66]–[68]. The vast majority of this work has dealt with geometries in which the mode propagates via total internal reflection or is confined by a metallic structure. The use of a tapered structure for the guided propagation of a surface wave or surface plasmon polariton is a more recent development [65], [69], [70]. The treatment of Sommerfeld waves developed by Goubau indicates that the lateral extent of the electric field decreases with decreasing wire diameter, but a nontrivial analytical expression defining this relation does not exist [46]. The rate of decrease in the field extent seen in our simulations of adiabatically tapered waveguides must be characterized and compared to this analytic expression. Clearly, FEM simulations play an important role in the

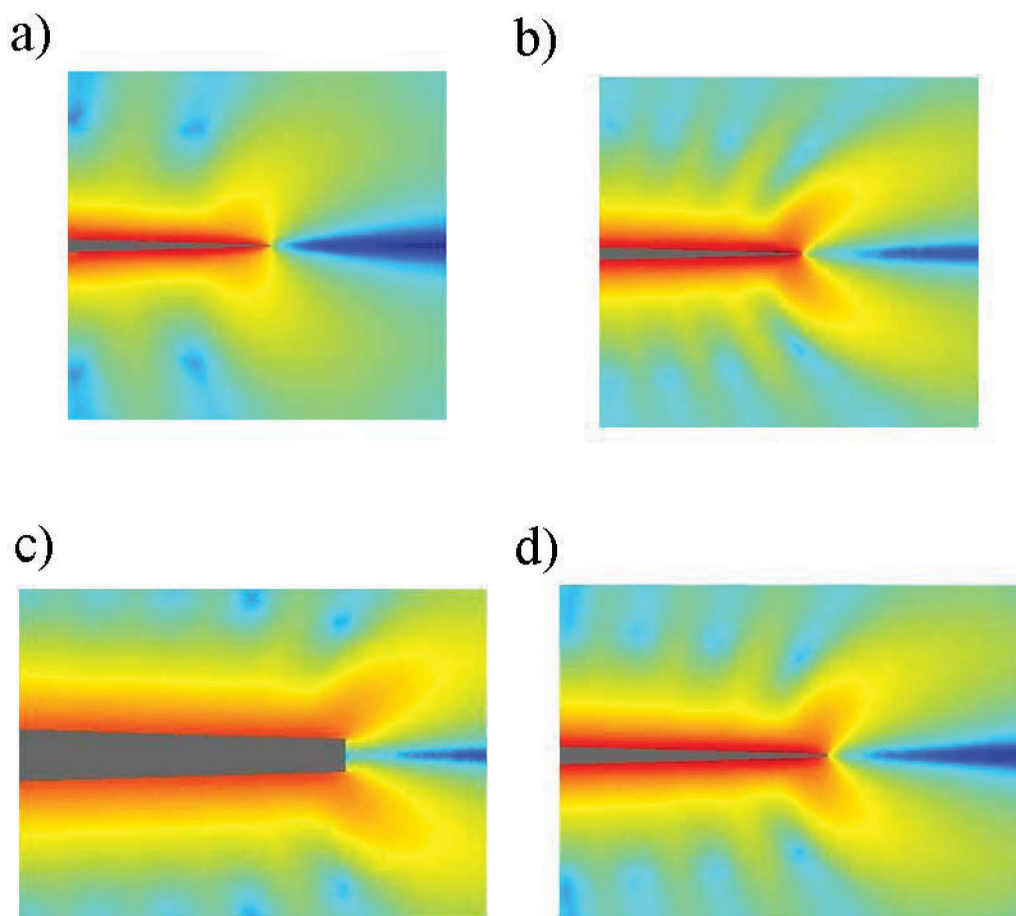


Fig. 15. FEM simulation results showing the power (log scale) wave propagating to the end of a tapered wire waveguide for differing tip diameters and frequencies. (a) 20 μm tip diameter at a frequency of 100 GHz. (b) 20 μm tip diameter at a frequency of 200 GHz. (c) 500 μm tip diameter at a frequency of 150 GHz. (d) 50 μm tip diameter at a frequency of 150 GHz.

ongoing study of tapered surface plasmon polariton waveguides.

VI. CONCLUDING REMARKS

The use of cylindrical metal wires as terahertz waveguides provides a low attenuation and virtually dispersionless method of guiding and manipulating pulsed terahertz radiation. In order to exploit terahertz metal wire waveguides, it is essential to characterize both the coupling of free-space THz radiation to the surface plasmon polaritons and also the radiation of this energy back into free-space at the end of the wire waveguide. We have shown that the FEM, used in conjunction with ongoing experimental measurements, is a powerful tool for the modeling of terahertz guided wave phenomena. The FEM has been used to simulate the coupling of linearly polarized terahertz radiation to a metal wire waveguide and to develop a novel photoconductive antenna source

that significantly improves the free-space to guided-mode coupling efficiency. In addition, FEM methods can describe the nature of the near-field to far-field transition at the end of wire waveguides, which helps to explain the strong spatial dependence of the measured pulse spectra.

In passing, we note that we have also made extensive use of the FEM to study the interaction of THz radiation with photonic crystals. Photonic crystals exhibit periodicity in their dielectric function in one or more dimensions [71], [72]. This periodicity can be tuned in order to manipulate the flow of optical radiation. Two-dimensional photonic crystals, consisting of periodic air holes etched in high resistivity silicon, have been fabricated for study with time-domain spectroscopy [73]–[75]. FEM simulations of the interaction of THz radiation with photonic crystals have been employed to calculate the transmission spectrum and showed excellent agreement with experimental results [73]. The FEM has also recently

been compared with experimental studies of superprism effects in terahertz photonic crystals [75].

The FEM can be employed as an effective computational tool to aid in the research and development associated with terahertz time-domain spectroscopy and imaging. FEM modeling of novel terahertz devices can save considerable research time and resources by tuning the design parameters prior to fabrication. FEM simulations of terahertz phenomena such as the propagation of terahertz radiation in or along novel waveguides or the

interaction of THz pulses with novel systems like photonic crystals can provide an increased understanding of the interaction, as well as useful feedback for the design of optimized devices. ■

Acknowledgment

The authors would like to Vincent Cocula and Magnus Olsson of COMSOL AB for their valuable scientific and technical advice.

REFERENCES

- [1] D. M. Mittleman et al., "Non-contact semiconductor wafer characterization with the terahertz hall effect," *Appl. Phys. Lett.*, vol. 71, pp. 16–18, 1997.
- [2] D. Grischkowsky et al., "Far-infrared time-domain spectroscopy with terahertz beams of dielectrics and semiconductors," *J. Opt. Soc. Amer. B*, vol. 7, no. 10, pp. 2006–2015, 1990.
- [3] D. Crawley et al., "Three-dimensional terahertz pulse imaging of dental tissue," *J. Biol. Opt.*, vol. 8, pp. 303–307, 2003.
- [4] R. M. Woodward et al., "Terahertz pulsed imaging of skin cancer in the time and frequency domain," *J. Biol. Phys.*, vol. 29, pp. 257–261, 2003.
- [5] R. H. Jacobson, D. M. Mittleman, and M. C. Nuss, "Chemical recognition of gases and gas mixtures using terahertz radiation," *Opt. Lett.*, vol. 21, pp. 2011–2013, 1996.
- [6] M. R. Leahy-Hoppa et al., "Wideband terahertz spectroscopy of explosives," *Chem. Phys. Lett.*, vol. 434, no. 4–6, pp. 227–230, 2007.
- [7] Y. C. Shen et al., "Detection and identification of explosives using terahertz pulsed spectroscopic imaging," *Appl. Phys. Lett.*, vol. 86, no. 24, p. 241 116, 1986.
- [8] K. Kawase, Y. Ogawa, and Y. Watanabe, "Non-destructive terahertz imaging of illicit drugs using spectral fingerprints," *Opt. Express*, vol. 11, no. 20, pp. 2549–2554, 2003.
- [9] F. Huang et al., "Terahertz study of 1, 3, 5-trinitro-s-triazine by time-domain and Fourier transform infrared spectroscopy," *Appl. Phys. Lett.*, vol. 85, no. 23, pp. 5535–5537, 2004.
- [10] D. Zimdars et al., "Large area terahertz imaging and non-destructive evaluation applications," *Insight—Non-Destr. Test. Cond. Monit.*, vol. 48, no. 9, pp. 537–539, 2006.
- [11] S. Wang and X.-C. Zhang, "Pulsed terahertz tomography," *J. Phys. D*, vol. 37, pp. R1–R36, 2004.
- [12] D. M. Mittleman, Ed., *Sensing With Terahertz Radiation*. Heidelberg, Germany: Springer-Verlag, 2002.
- [13] P. R. Smith, D. H. Auston, and M. C. Nuss, "Subpicosecond photoconducting dipole antennas," *IEEE J. Quantum Electron.*, vol. 24, no. 2, pp. 255–260, Feb. 1988.
- [14] M. v. Exter and D. Grischkowsky, "Characterization of an optoelectronic terahertz beam systems," *IEEE Trans. Microw. Theory Tech.*, vol. 38, no. 11, pp. 1684–1690, Nov. 1990.
- [15] X.-C. Zhang et al., "Terahertz optical rectification from a nonlinear organic crystal," *Appl. Phys. Lett.*, vol. 61, no. 26, pp. 3080–3082, 1992.
- [16] D. H. Auston and K. P. Cheung, "Coherent time-domain far-infrared spectroscopy," *J. Opt. Soc. Amer. B: Opt. Phys.*, vol. 2, no. 4, pp. 606–612, 1985.
- [17] Q. Wu and X.-C. Zhang, "Free-space electro-optic sampling of terahertz beams," *Appl. Phys. Lett.*, vol. 67, no. 24, pp. 3523–3525, 1995.
- [18] K. Wang and D. M. Mittleman, "Guided propagation of terahertz pulses on metal wires," *J. Opt. Soc. Amer. B*, vol. 22, pp. 2001–2007, 2005.
- [19] M. Goto et al., "Teflon photonic crystal fiber as terahertz waveguide," *Jpn. J. Appl. Phys.*, vol. 43, pp. L317–L319, 2004.
- [20] H. Han et al., "Terahertz pulse propagation in a plastic photonic crystal fiber," *Appl. Phys. Lett.*, vol. 80, pp. 2634–2636, 2002.
- [21] G. d. l. Reyes et al., "Low-loss single-mode terahertz waveguiding using Cytop," *Appl. Phys. Lett.*, vol. 89, p. 211 119, 2006.
- [22] S. A. Maier and H. A. Atwater, "Plasmonics: Localization and guiding of electromagnetic energy in metal/dielectric structures," *J. Appl. Phys.*, vol. 98, p. 011 101, 2005.
- [23] R. Mendis and D. Grischkowsky, "Undistorted guided-wave propagation of subpicosecond terahertz pulses," *Opt. Lett.*, vol. 26, no. 11, pp. 846–848, 2001.
- [24] R. Mendis and D. Grischkowsky, "THz interconnect with low-loss and low-group velocity dispersion," *IEEE Microw. Wireless Compon. Lett.*, vol. 11, no. 11, pp. 444–446, Nov. 2001.
- [25] M. Nagel, A. Marchewka, and H. Kurz, "Low-index discontinuity terahertz waveguides," *Opt. Express*, vol. 14, no. 21, pp. 9944–9954, 2006.
- [26] M. Wachter, M. Nagel, and H. Kurz, "Metallic slit waveguide for dispersion-free low-loss terahertz signal transmission," *Appl. Phys. Lett.*, vol. 90, p. 061 111, 2007.
- [27] K. Wang and D. M. Mittleman, "Metal wires for terahertz waveguiding," *Nature*, vol. 432, p. 376, 2004.
- [28] M. Wachter, M. Nagel, and H. Kurz, "Frequency-dependent characterization of THz Sommerfeld wave propagation on single-wires," *Opt. Express*, vol. 13, no. 26, p. 10 815, 2005.
- [29] T.-I. Jeon and D. Grischkowsky, "Direct optoelectronic generation and detection of sub-ps-electrical pulses on sub-mm-coaxial transmission lines," *Appl. Phys. Lett.*, vol. 85, no. 25, pp. 6092–6094, 2004.
- [30] R. Coccioli et al., "Finite-element methods in microwaves: A selected bibliography," *IEEE Antennas Propag. Mag.*, vol. 38, no. 6, pp. 34–38, Dec. 1996.
- [31] B. M. A. Rahman, F. A. Fernandez, and J. B. Davies, "Review of finite element methods for microwave and optical waveguides," *Proc. IEEE*, vol. 79, no. 10, pp. 1442–1448, Oct. 1991.
- [32] I. Tsukerman, F. Cajko, and A. P. Sokolov, "Traditional and new simulation techniques for nanoscale optics and photonics," *Proc. SPIE, Plasmonics: Metallic Nanostructures and Their Optical Properties III*, vol. 5927, pp. 128–137, 2005.
- [33] R. L. Courant, "Variational methods for the solution of problems of equilibrium and vibration," *Bulletin of the American Mathematical Society*, vol. 5, pp. 1–23, 1943.
- [34] P. P. Silvester, "Finite-element solution of homogeneous waveguide problems," *Alta Frequenza*, vol. 38, pp. 313–317, 1969.
- [35] W. B. J. Zimmerman, *Multiphysics Modeling With Finite Element Methods*, ser. Series on Stability, Vibration, and Control of Systems, Series A. London: World Scientific, 2006, vol. 18.
- [36] J. Jin, *The Finite Element Method in Electromagnetics*. New York: John Wiley & Sons, Inc., 2002.
- [37] C. Ashcraft, SPOOLERS.
- [38] T. Davis, UMFPAK, Gainesville, FL, 2005.
- [39] R. Barrett et al., *Templates for the Solution of Linear Systems: Building Blocks for Iterative Methods*, ser. Miscellaneous Titles in Applied Mathematics Series No. 43. Philadelphia: SIAM, 1994.
- [40] D. Jiao and J.-M. Jin, "A general approach for the stability analysis of the time-domain finite-element method for electromagnetic simulations," *IEEE Trans. Antennas Propag.*, vol. 50, no. 11, pp. 1624–1632, Nov. 2002.
- [41] J.-F. Lee, R. Lee, and A. Cangelaris, "Time-domain finite-element methods," *IEEE Trans. Antennas Propag.*, vol. 45, no. 3, pp. 430–441, Mar. 1997.
- [42] B. Butrylo et al., "A survey of parallel solvers for the finite element method in computational electromagnetics," *COMPEL: The International J. for Computation and Mathematics in Electrical and Electronic Engineering*, vol. 23, no. 2, pp. 531–546, 2004.
- [43] O. Schenk and K. Gartner, "On fast factorization pivoting methods for symmetric indefinite systems," *Elec. Trans. Numer. Anal.*, vol. 23, pp. 158–179, 2006.
- [44] O. Schenk and K. Gartner, "Solving unsymmetric sparse systems of linear equations with PARDISO," *J. Future Generation Computer Systems*, vol. 20, no. 3, pp. 475–487, 2004.
- [45] COMSOL Multiphysics. Stockholm, Sweden: COMSOL AB, 2007.

- [46] G. Goubau, "Surface waves and their application to transmission lines," *J. Appl. Phys.*, vol. 21, pp. 1119–1128, 1950.
- [47] T.-I. Jeon, J. Zhang, and D. Grischkowsky, "THz Sommerfeld wave propagation on a single metal wire," *Appl. Phys. Lett.*, vol. 86, p. 161 904, 2005.
- [48] Q. Cao and J. Jahns, "Azimuthally polarized surface plasmons as effective terahertz waveguides," *Opt. Express*, vol. 13, no. 2, pp. 511–518, 2005.
- [49] K. L. Shlager, G. S. Smith, and J. G. Maloney, "Optimization of bow-tie antennas for pulse radiation," *IEEE Trans. Antennas Propag.*, vol. 42, no. 7, pp. 975–982, Jul. 1994.
- [50] D. B. Rutledge, D. P. Neikirk, and D. P. Kasilingam, "Integrated-circuit antennas," in *Infrared and Millimeter Waves*, K. J. Button, Ed. New York: Academic, 1983, pp. 1–90.
- [51] J. V. Rudd and D. M. Mittleman, "The influence of substrate lens design in terahertz time-domain spectroscopy," *J. Opt. Soc. Amer. B*, vol. 19, pp. 319–329, 2002.
- [52] Y. Zhu and A. Cangellaris, *Multigrid Finite Element Methods for Electromagnetic Field Modeling*, ser. The IEEE Press Series on Electromagnetic Wave Theory, D. G. Dudley, Ed. Hoboken, NJ: Wiley, Inc., 2006.
- [53] J. A. Deibel et al., "Enhanced coupling of terahertz radiation to cylindrical wire waveguides," *Opt. Express*, vol. 14, pp. 279–290, 2006.
- [54] F. Yang, J. R. Sambles, and G. W. Bradberry, "Long-range surface modes supported by thin films," *Phys. Rev. B*, vol. 44, pp. 5855–5572, 1991.
- [55] J. V. Rudd, J. L. Johnson, and D. M. Mittleman, "Cross-polarized angular emission patterns from lens-coupled terahertz antennas," *J. Opt. Soc. Amer. B*, vol. 18, pp. 1524–1533, 2001.
- [56] H. Cao and A. Nahata, "Coupling of terahertz pulses onto a single metal wire waveguide using milled grooves," *Opt. Express*, vol. 13, no. 18, pp. 7028–7034, 2005.
- [57] J. Deibel, M. Escarra, and D. M. Mittleman, "Photoconductive terahertz antenna with radial symmetry," *Electron. Lett.*, vol. 41, pp. 9–10, 2005.
- [58] J. D. Jackson, *Classical Electrodynamics*, 3rd ed. New York: Wiley, 1999.
- [59] P. U. Jepsen and S. R. Keiding, "Radiation patterns from lens coupled terahertz antennas," *Opt. Lett.*, vol. 20, no. 8, pp. 807–809, 1995.
- [60] C. Fattinger and D. Grischkowsky, "Terahertz beams," *Appl. Phys. Lett.*, vol. 54, pp. 490–492, 1989.
- [61] G. Chang et al., "Generation of radially polarized terahertz pulses via velocity-mismatched optical rectification," *Opt. Lett.*, vol. 32, no. 4, pp. 433–435, 2007.
- [62] M. Walther et al., "Emission and detection of terahertz pulses from a metal-tip antenna," *J. Opt. Soc. Amer. B*, vol. 22, pp. 2357–2365, 2005.
- [63] M. Walther, M. R. Freeman, and F. A. Hegmann, "Metal-wire terahertz time-domain spectroscopy," *Appl. Phys. Lett.*, vol. 87, p. 261 107, 2005.
- [64] J. A. Deibel et al., "Frequency-dependent radiation patterns emitted by THz plasmons on finite length cylindrical wires," *Opt. Express*, vol. 14, pp. 8772–8778, 2006.
- [65] S. A. Maier et al., "Terahertz surface plasmon-polariton propagation and focusing on periodically corrugated metal wires," *Phys. Rev. Lett.*, vol. 97, p. 176 805, 2006.
- [66] K. Matsumaru, "Reflection of a pyramidally tapered rectangular waveguide," *IRE Trans. Microw. Theory Tech.*, vol. MTT-7, no. 2, pp. 192–196, Apr. 1959.
- [67] F. Sporleder and H.-G. Unger, *Waveguide Tapers, Transitions, & Couplers*, ser. IEE Electromagnetic Waves Series. London, U.K.: IEE, 1979.
- [68] N. N. Qaddoumi, M. Abou-Khousa, and W. M. Saleh, "Near-field microwave imaging utilizing tapered rectangular waveguides," *IEEE Trans. Instrum. Meas.*, vol. 55, no. 5, pp. 1752–1756, Oct. 2006.
- [69] D. F. P. Pile and D. K. Gramotnev, "Adiabatic and nonadiabatic nanofocusing of plasmons by tapered waveguides," *Appl. Phys. Lett.*, vol. 89, p. 041 111, 2006.
- [70] M. I. Stockman, "Nanofocusing of optical energy in tapered plasmonic waveguides," *Phys. Rev. Lett.*, vol. 93, no. 13, p. 137 404, 2004.
- [71] S. John, "Strong localization of photons in certain disordered dielectric superlattices," *Phys. Rev. Lett.*, vol. 58, pp. 2486–2489, 1987.
- [72] E. Yablonovitch, "Inhibited spontaneous emission in solid-state physics and electronics," *Phys. Rev. Lett.*, vol. 58, pp. 2059–2062, 1987.
- [73] Z. Jian and D. M. Mittleman, "Characterization of guided resonances in photonic crystal slabs using terahertz time-domain spectroscopy," *J. Appl. Phys.*, vol. 100, p. 123 113, 2006.
- [74] Z. Jian and D. M. Mittleman, "Out-of-plane dispersion and homogenization in photonic crystal slabs," *Appl. Phys. Lett.*, vol. 87, p. 191 113, 2005.
- [75] T. Prasad et al., "The superprism effect in a metal-clad terahertz photonic crystal slab," *Opt. Lett.*, vol. 32, pp. 683–685, 2007.

ABOUT THE AUTHORS

Jason A. Deibel (Member, IEEE) was born in Louisville, KY, in 1974. He received the B.A. degree in physics and mathematics from Transylvania University, Lexington, KY, in 1997 and the Ph.D. degree in applied physics from the University of Michigan, Ann Arbor in 2004.

From 1997 to 2004, he was a Graduate Student Research Assistant in the Ultrafast Technology Group at the University of Michigan Center for Ultrafast Optical Science. Since 2004, he has been a Postdoctoral Research Associate in the Department of Electrical and Computer Engineering at Rice University, Houston, TX, where he is a member of Professor Daniel Mittleman's research group. He was an Intelligence Community Postdoctoral Fellow from 2004–2007. He spent two months in 2006 at the University of Leeds, U.K., as a Royal Society Visiting Fellow. He will join the Department of Physics as an Assistant Professor at Wright State University, Dayton, OH, in Fall 2007. His research interests include terahertz transmission and emission spectroscopy of novel inorganic and organic semiconductors, terahertz microscopy and plasmonics, terahertz waveguide development, and finite-element method simulations of terahertz radiation phenomena and devices.

Dr. Deibel is a member of the Optical Society of America, the American Physical Society, and the IEEE Lasers and Electro-Optics Society.



Matthew Escarra (Student Member, IEEE) was born in New Orleans, LA, in 1984. He received the B.S. degree in electrical engineering from Rice University, Houston, TX, in 2006. He is currently working toward the Ph.D. degree in the Department of Electrical Engineering, Princeton University, Princeton, NJ.

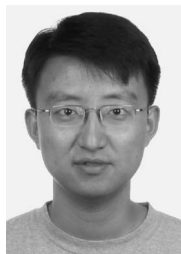
As an undergraduate at Rice, he was involved in the development of a new generation of photoconductive terahertz antennas for use with metal wire waveguides. As a graduate student at Princeton, he is a member of Professor Claire Gmachl's Mid-Infrared Photonics research group, a part of the Mid-Infrared Technologies for Health and the Environment (MIRTHE) NSF Engineering Research Center.

Nicholas Berndsen (Student Member, IEEE) was born in St. Louis, MO, in 1985. He is currently working toward the B.S. degree in electrical engineering at Rice University, Houston, TX, and will graduate in 2008.

He is a member of Professor Daniel Mittleman's research group and is also a Co-President of the 2007–2008 Rice chapter of the IEEE.



Kanglin Wang received the B.S. degree in applied physics from Tongji University, China, in 1998, the M.S. degree in physics from Fudan University, China in 2001, and the Ph.D. degree in applied physics from Rice University, Houston, TX, in 2006.



From 2001 to 2006, he was a graduate student in the Department of Electrical and Computer Engineering at Rice University, and studied novel devices and systems for terahertz spectroscopy and imaging in professor Daniel Mittleman's research group. He then joined Shell Oil Company, Houston, TX, and took a research position in the Potential Field and Remote Sensing team.

Daniel M. Mittleman (Member, IEEE) was born in Berkeley, CA, in 1966. He received the B.S. degree in physics from the Massachusetts Institute of Technology, Cambridge, in 1988 and the M.S. and Ph.D. degrees in physics from the University of California, Berkeley, in 1990 and 1994, respectively.



He spent two years as a Postdoctoral Member of the Technical Staff at AT&T Bell Laboratories (now Lucent Technologies), where he was involved in the development of terahertz "T-ray" imaging. In 1996, he joined the faculty of the Electrical and Computer Engineering Department at Rice University, Houston, TX, where he is now an Associate Professor. His research involves ultrafast optoelectronic generation of terahertz radiation and its applications for spectroscopy and imaging. He is also active in the study of new terahertz techniques, devices, and systems.

Prof. Mittleman is a member of the Optical Society of America, the American Physical Society, and the IEEE Lasers and Electro-Optics Society. He is the Founder and Chair of the Houston chapter of IEEE/LEOS.